

Supporting information for

Near Room Temperature Stepwise Spin State Switching and Photomagnetic Effect in a Mixed-Valence Molecular Square

Sujit Kamilya,^a Sakshi Mehta,^a Rodrigue Lescouëzec,^b Yanling Li,^b Jiri Pechousek,^c Mohini Semwal,^a
and Abhishake Mondal*^a

^a*Solid State and Structural Chemistry Unit, Indian Institute of Science, Sir C. V. Raman Road, Bangalore-560012, India. Email: mondal@iisc.ac.in, <http://m2ssscuiisc.in>.*

^b*Sorbonne Université, Institut Parisien de Chimie Moléculaire, UMR CNRS 8232, 4 place Jussieu, Paris 750005, France.*

^c*Department of Experimental Physics, Palacký University Olomouc, 17. listopadu 1192/12, 771 46 Olomouc, Czech Republic.*

Email: mondal@iisc.ac.in

Table of contents:

1. Experimental techniques
 - i. Crystal structure analyses
 - ii. Magnetic measurements
 - iii. Other physical measurements
2. References

List of Figures

Fig. S1 Thermogravimetric analysis plot for 1·4MeOH·2H ₂ O.	6
Fig. S2 Comparison of the room temperature (300 K) experimental PXRD pattern and the simulated one for 1·4MeOH·2H ₂ O at 296 K (top) and at 120 K (bottom) respectively.	6
Fig. S3 DSC plot of 1·4MeOH·2H ₂ O (left) and 1 (right) shown between 300 and 400 K at 15 K/min sweep rate.	7
Fig. S4 Perspective view of asymmetric unit of 1·4MeOH·2H ₂ O (Fe(II), orange; Fe(III), yellow; C, gray; N, blue; O, red and B, light pink). H-atoms are omitted for clarity.	7
Fig. S5 Perspective view of unit cell in 1·4MeOH·2H ₂ O (Fe(II), orange; Fe(III), yellow; C, gray; N, blue; O, red and B, light pink). H-atoms are omitted for clarity.	8
Fig. S6 Perspective view of H-bonding OH···N interaction in 1·4MeOH·2H ₂ O. The green and magenta dotted line represent H-bonding interactions involved with H ₂ O and MeOH respectively. (Fe(II), orange; Fe(III), yellow; C, gray; N, blue; O, red and B, light pink). Atoms shown in wireframe style are for clarity. H-atoms other than H-bonding interactions are omitted for clarity.	8
Fig. S7 Perspective view of crystal packing in 1·4MeOH·2H ₂ O showing supramolecular interactions (C-H···C, C-H···N, C-H···O, π-π stacking) between square motifs. π-π stacking between pyrazole rings of pzTp ligands showed in black dotted line (3.633 Å) through yellow colored centroid. CH···π interactions among counter anions are presented in black dotted line with 3.576 Å distance. Magenta and blue dotted line are the H-bonding interactions involving MeOH and H ₂ O respectively. H-atoms are omitted for clarity.	9
Fig. S8 The first derivative of χT against the temperature, $d(\chi T) / dT$ vs. T in the temperature range of 100 K to 400 K for 1·4MeOH·2H ₂ O and 1 (from left to right).	9
Fig. S9 M vs H plot for 1·4MeOH·2H ₂ O (red curve) and 1 (blue curve) measured at 2 K. The solid lines are guide for the eyes.	10
Fig. S10 χT vs. T plots of 1 before and after the 808 nm light irradiation for 230 min at 20 K, 2500 Oe dc field while heating the sample with 0.5 K/min sweep rate.	10
Fig. S11 χT vs. time plots of the photo-induced metastable state of 1 under the 532 nm (green) and 405 nm (blue) laser light irradiation.	11
Fig. S12 M vs. H curves of 1 at 2 K before irradiation (black) and after irradiation with 405 nm (blue), 532 nm (green), 635 nm (red), 808 nm (dark red) laser light irradiation at 20 K. The solid lines are guide for the eyes.	11
Fig. S13 Solid state FT-IR spectra of 1·4MeOH·2H ₂ O and 1 in ATR mode in the region of 4000 to 550 cm ⁻¹ at room temperature (300 K).	12
Fig. S14 Variable temperature solid state FT-IR spectra of 1·4MeOH·2H ₂ O in the temperature range of 310 K – 420 K from 4000 to 550 cm ⁻¹ in KBr pellet. Left: Heating mode, and right: cooling mode. Upward and downward arrows signify the heating and cooling mode respectively.	12
Fig. S15 Variable temperature solid state FT-IR spectra of 1 in the temperature range of 310 K – 420 K from 4000 to 550 cm ⁻¹ in KBr pellet. Left: Heating mode, and right: cooling mode. Upward and downward arrows signify the heating and cooling mode respectively.	13
Fig. S16 Variable temperature solid state FT-IR spectra of 1·4MeOH·2H ₂ O in the temperature range of 310 K – 420 K from 2250 to 2050 cm ⁻¹ in KBr pellet in cooling mode. Upward and downward arrows signify the heating and cooling mode, respectively.	13
Fig. S17 Variable temperature solid state FT-IR spectra of 1 in the temperature range of 310 K – 420 K from 2250 to 2050 cm ⁻¹ in KBr pellet method. Left: Heating mode, and right: cooling mode. Upward and downward arrows signify the heating and cooling mode, respectively.	14
Fig. S18 Variable temperature solid state FT-IR spectra of 1·4MeOH·2H ₂ O in the temperature range of 310 K – 420 K from 1700 to 1600 cm ⁻¹ in KBr pellet. Left: Heating mode, and right: cooling mode. Upward and downward arrows signify the heating and cooling mode, respectively.	14
Fig. S19 Variable temperature solid state FT-IR spectra of 1 in the temperature range of 310 K – 420 K from 1700 to 1600 cm ⁻¹ in KBr pellet. Left: Heating mode, and right: cooling mode. Upward and downward arrows signify the heating and cooling mode, respectively.	15

Fig. S20 Variable temperature solid state FT-IR spectra of 1 ·4MeOH·2H ₂ O in the temperature range of 310 K – 420 K from 1440 to 1400 cm ⁻¹ in KBr pellet. Left: Heating mode, and right: cooling mode. Upward and downward arrows signify the heating and cooling mode, respectively.....	15
Fig. S21 Variable temperature solid state FT-IR spectra of 1 in the temperature range of 310 K – 420 K from 1440 to 1400 cm ⁻¹ in KBr pellet method. Left: Heating mode, and right: cooling mode. Upward and downward arrows signify the heating and cooling mode, respectively.....	15
Fig. S22 Compared solution state UV/vis/NIR spectra of 1 ·4MeOH·2H ₂ O in different solvents with concentration of ≈ 10 ⁻⁴ (M) at RT (300 K) (left) and solution state UV/vis/NIR spectrum of [Fe ^{II} (bik*) ₃](BF ₄) ₂ (right).	16
Fig. S23 Mössbauer spectrum of 1 ·4MeOH·2H ₂ O at 330 K. The green, blue and red curves represent the quadrupole doublets of the LS-Fe(III), LS-Fe(II) and HS-Fe(II) ions, respectively.	16
Fig. S24 Mössbauer spectrum of 1 at 300 K (left) and 350 K (right). The green, blue and red curves represent the quadrupole doublets of the LS-Fe(III), LS-Fe(II) and HS-Fe(II) ions, respectively	17
Fig. S25 Cyclic voltammograms of 1 ·4MeOH·2H ₂ O for reduction cycle (left) and oxidation cycle (right) in 0.1 M TBAPF ₆ /acetonitrile with different scan rate. Arrows indicate the direction of the potential sweep.	17
Fig. S26 Cyclic voltammogram of (PPh ₄)[Fe ^{III} (pzTp)(CN) ₃] in 0.1 M TBAPF ₆ /acetonitrile with a scan rate of 0.1 V s ⁻¹	18
Fig. S27 Square wave voltammograms for 1 ·4MeOH·2H ₂ O in 0.1 M (TBA)PF ₆ /acetonitrile. Arrows indicate the direction of potential sweep.....	18

List of Tables

Table S1 X-ray Crystallography data of 1 ·4MeOH·2H ₂ O.....	19
Table S2 CShM analyses data for 1 ·4MeOH·2H ₂ O.....	20
Table S3 Octahedral distortion parameter calculation for 1 ·4MeOH·2H ₂ O.....	20
Table S4 Selected bond lengths (Å) in 1 ·4MeOH·2H ₂ O.	21
Table S5 Selected bond angles (°) in 1 ·4MeOH·2H ₂ O at 120 K.....	22
Table S6 Mössbauer spectroscopy data for 1 ·4MeOH·2H ₂ O and 1 at different temperatures.	24

1. Experimental techniques:

Materials: All reagents were obtained from commercial suppliers and were used without further purification unless otherwise noted. The cyanide building blocks $(\text{PPh}_4)[\text{Fe}^{\text{III}}(\text{pzTp})(\text{CN})_3]\cdot\text{H}_2\text{O}$ and the ligand bik* (bik* = bis(1-ethyl-1*H*-imidazol-2-yl)ketone) were prepared according to the modified literature procedures.^{1,2} The detailed physical methods were performed using a similar procedure described by Mondal *et. al.*³

$\{[\text{Fe}(\text{pzTp})(\text{CN})_3]_2[\text{Fe}(\text{bik}^*)_2]\}[\text{Fe}(\text{pzTp})(\text{CN})_3]_2\cdot 4\text{MeOH}\cdot 2\text{H}_2\text{O}$ (1·4MeOH·2H₂O): The reaction mixture of anhydrous FeCl₂ (12.6 mg, 0.1 mmol) and bik* (44.0 mg, 0.2 mmol) in dry methanol (10 mL) produces a blue color solution. After 10 min, this solution was added dropwise into $(\text{PPh}_4)[\text{Fe}^{\text{III}}(\text{pzTp})(\text{CN})_3]\cdot\text{H}_2\text{O}$ (78.8 mg, 0.1 mmol) solution. The resulting dark greenish black color solution was filtered and kept for crystallization by slow evaporation. After 3 days, dark red colored rectangular block type crystals were obtained (yield: 60 %). **1** was prepared by heating the crystals of 1·4MeOH·2H₂O in a Schlenk tube under argon atmosphere at 370 K. Formula for 1·4MeOH·2H₂O: C₁₀₈H₁₂₄B₄Fe₆N₆₀O₁₀ (MW: 2800.9 gmol⁻¹) Anal. Calcd.: C, 46.31; H, 4.46; N, 30.01. found: C, 45.72; H, 5.23; N, 31.02. IR (ATR, cm⁻¹): 3418, 3129, 2981, 2934, 2872, 2147, 2138, 2120, 1640, 1517, 1501, 1476, 1441, 1408, 1387, 1300, 1258, 1209, 1186, 1107, 1063, 924, 854, 787, 762, 665, and 615.

i. Crystal structure analyses:

Single crystal of complex 1·4MeOH·2H₂O were mounted on crystal mounting loop with the help of immersion oil and measured at 120 K. Diffraction data were collected using a Bruker SMART APEX II ULTRA diffractometer, equipped with a CCD type area detector with graphite-monochromated Mo-K α radiation ($\lambda = 0.71073 \text{ \AA}$). Data collection was performed with APEX2 suite (Bruker). Unit-cell parameters refinement, data integration and reduction were done by using SAINT program and absorption correction was done by SADABS program.⁴ Structures were solved using direct methods and refined with a full-matrix least-squares method on F^2 using SHELXL-2018⁵ program suite in OLEX 2 version 1.3.0.⁶ All non-hydrogen atoms were refined using anisotropic displacement parameters. Hydrogen atoms were labeled to ideal positions and refined isotropically using a riding model. Crystallographic data and refinement parameters are listed in Table S1. Selected bond distances and angles are listed in Table S4-S5, respectively. Further details may be obtained from the Cambridge Crystallographic Data Centre (CCDC) using www.ccdc.cam.ac.uk/deposit. CCDC entries 2252523 contain the supplementary crystallographic data for this article.

ii. Magnetic Measurements:

The magnetic susceptibility measurements were performed with Quantum Design MPMS-XL SQUID magnetometer, between 1.9 K to 400 K for dc applied fields ranging from -7 to +7 T. Polycrystalline sample of 1·4MeOH·2H₂O (20.71 mg) was introduced at 200 K in a polyethylene bag and was subjected to measurement. The temperature dependent data were measured using 2500 Oe dc magnetic field. M vs H measurements were performed at 100 K to check for the presence of ferromagnetic impurities which were found to be absent. The magnetic data were corrected for the sample holder and the diamagnetic contribution.

(Photo)Magnetic measurements were carried out for **1** by using a sample holder inside the Quantum Design MPMS-XL EverCool SQUID magnetometer equipped with an optical fiber. In a typical experiment 1.5 mg of finely ground crystals were deposited on an adhesive tape. The sample was separated from the end of the optical fiber by 5.5 cm. All the irradiations were carried out at 20

K to minimize the temperature variation induced by the light irradiation. The experimental data were corrected for the diamagnetic contribution of the constituent atoms as well as by the residual diamagnetic signal from the holder. Different Laser sources were also used in the visible range in order to improve the photoinduced effect (ranging from 405 nm, 532 nm, and 808 nm with powers of 5, 8 and 10 mW/cm²). Note that the temperatures have been corrected to consider the light irradiation heating (an average +2 K has been observed with 405 nm, 532 nm and 808 nm light). It is important to mention that the 635 nm diode laser light produces higher power (>50 mW/cm²) compared to other three laser lights and sometimes we are unable to stabilize the measurement temperature in the SQUID magnetometer at 20 K using 635 nm laser light. Experimental susceptibilities were corrected for sample holder and intrinsic diamagnetic contributions.

iii. Other physical measurements:

The crystals of the complex were removed from the mother liquor and dried on filter paper to remove any adhering solvent, prior to measurement. The elemental analyses of C, H and N were performed with Thermo Scientific Flash 2000 Organic Elemental Analyzer. Infrared (IR) spectra were recorded in the range of 4000–400 cm⁻¹ on PerkinElmer FT-IR Frontier spectrometer. UV/vis/NIR spectra were carried out in the region of 250 – 2000 nm on a PerkinElmer Lambda 1050+ UV/vis/NIR spectrometer. The UV/vis spectroscopic measurements in solution were done in quartz cuvettes with a path length of 1 cm in the region of 250 – 1200 nm. Solid-state measurements were carried out by taking 5 % sample by weight in KBr. Thermogravimetric analysis (TGA) was done on a Mettler Toledo TGA/SDTA851 analyzer with a heating rate of 5 K min⁻¹ under a nitrogen atmosphere ranging from 300 K to 600 K. Differential scanning calorimetry (DSC) measurements were performed using Mettler Toledo DSC 823^e differential scanning calorimeter with a scan rate of 5 K min⁻¹ in a nitrogen atmosphere. Powder X-ray diffraction (PXRD) measurements were carried out on a PANalytical Empyrean diffractometer at 45 kV and 30 mA, under Cu-K_α radiation ($\lambda = 1.54059 \text{ \AA}$). PXRD data analyses were done using PANalytical X'Pert HighScore Plus software.⁷ Electrochemical measurements were performed using three electrode setup in potentiostat Metrohm Autolab PGSTAT101. The three electrodes are as follows: Ag/AgCl reference electrode, platinum working electrode and platinum wire as counter electrode. All the experiments were performed in acetonitrile solvent with *ca.* 1 mM of sample concentration and 0.1 M TBAPF₆ as supporting electrolyte with different scan rate at 300 K. Before each experiment the whole solution was purged with nitrogen and all the experiments were done under nitrogen atmosphere to avoid the oxygen from dissolving into the solution. Ferrocene was used as an internal reference. The ⁵⁷Fe Mössbauer spectra with 512 channels were measured employing a laboratory Mössbauer spectrometer,⁹ operating at a constant acceleration mode and equipped with a ⁵⁷Co(Rh) source. The Mössbauer spectra were fitted using the MossWinn (version 4.0) software program.¹⁰ The isomer shift values were referred to α -Fe foil sample at room temperature. The variable temperature measurements were recorded at 100 K, 300 K, 330 K and 350 K respectively using a Cryostation (Montana Instruments) closed-cycle cryogen-free system on which a Mössbauer spectrometer was fixed.

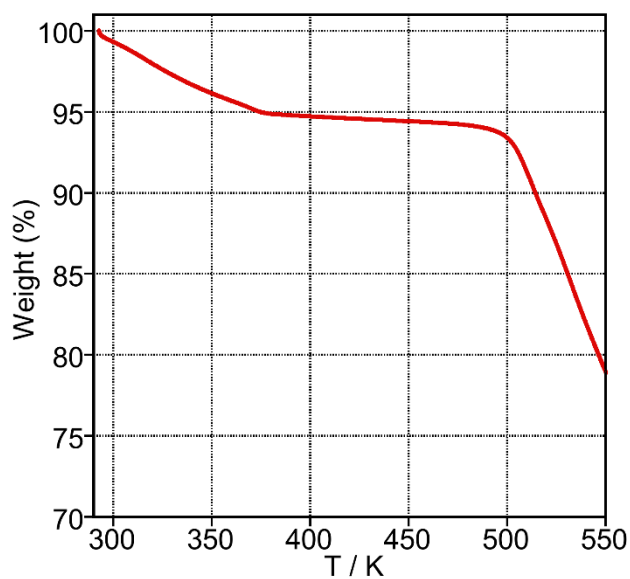


Fig. S1 Thermogravimetric analysis plot for $1 \cdot 4\text{MeOH} \cdot 2\text{H}_2\text{O}$.

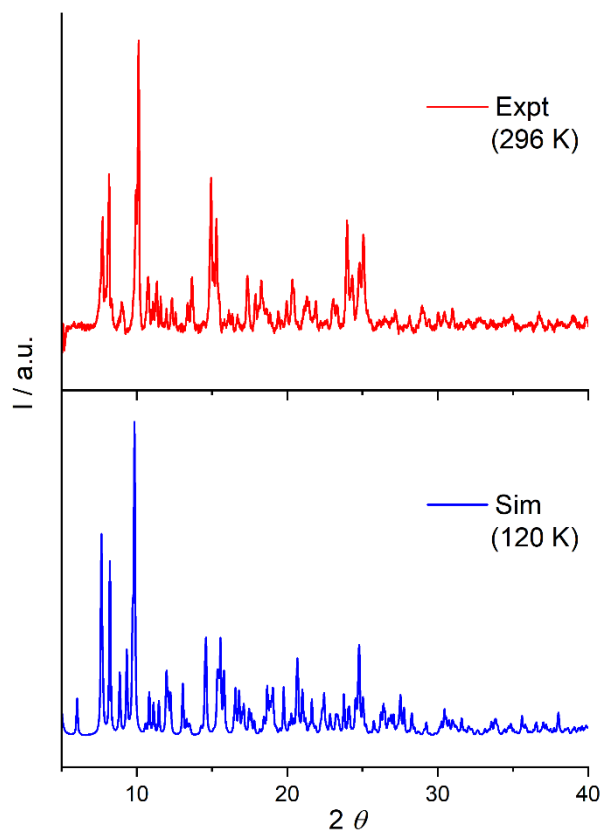


Fig. S2 Comparison of the room temperature (300 K) experimental PXRD pattern and the simulated one for $1 \cdot 4\text{MeOH} \cdot 2\text{H}_2\text{O}$ at 296 K (top) and at 120 K (bottom) respectively.

Note: The experimental powder XRD pattern was collected at 296 K and the simulated pattern was obtained from 120 K data. This complex loses its crystallinity by losing its lattice solvent molecules immediately after removing from its mother liquor. The lattice solvent loss and temperature difference in the PXRD experiment might causes the deviation from its simulated powder patterns.

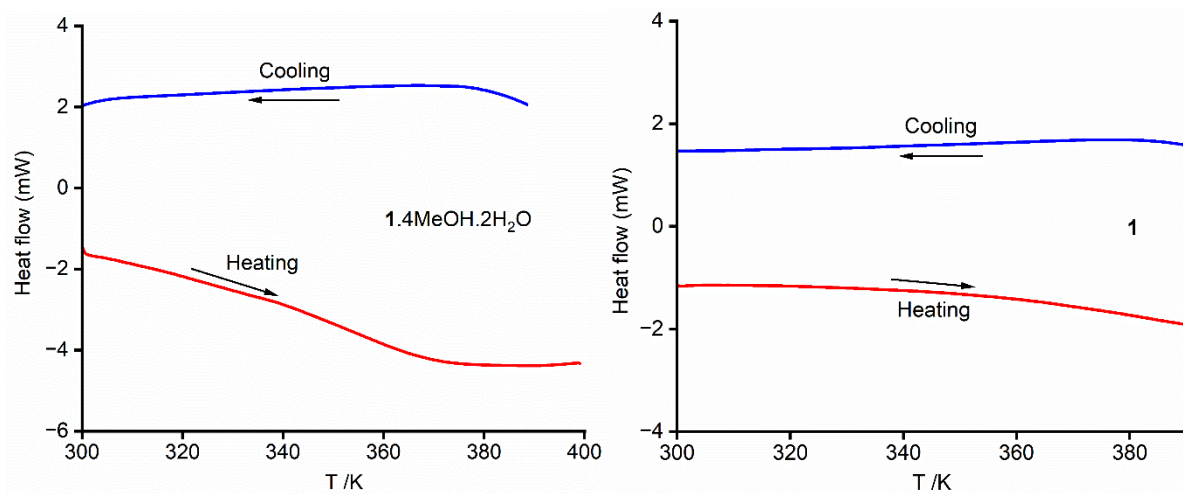


Fig. S3 DSC plot of **1**·4MeOH·2H₂O (left) and **1** (right) shown between 300 and 400 K at 15 K/min sweep rate.

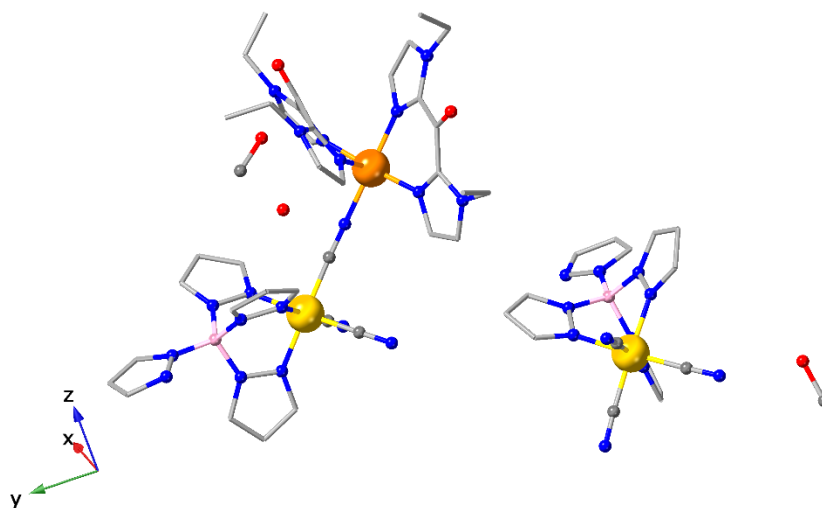


Fig. S4 Perspective view of asymmetric unit of **1**·4MeOH·2H₂O (Fe(II), orange; Fe(III), yellow; C, gray; N, blue; O, red and B, light pink). H-atoms are omitted for clarity.

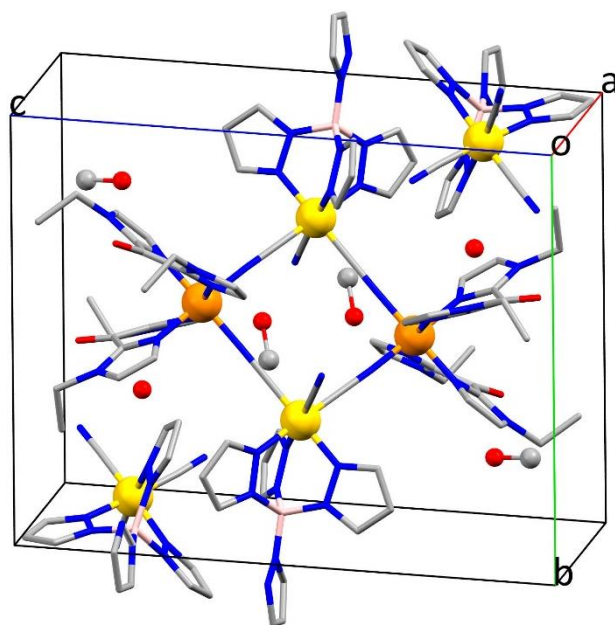


Fig. S5 Perspective view of unit cell in $1 \cdot 4\text{MeOH} \cdot 2\text{H}_2\text{O}$ (Fe(II), orange; Fe(III), yellow; C, gray; N, blue; O, red and B, light pink). H-atoms are omitted for clarity.

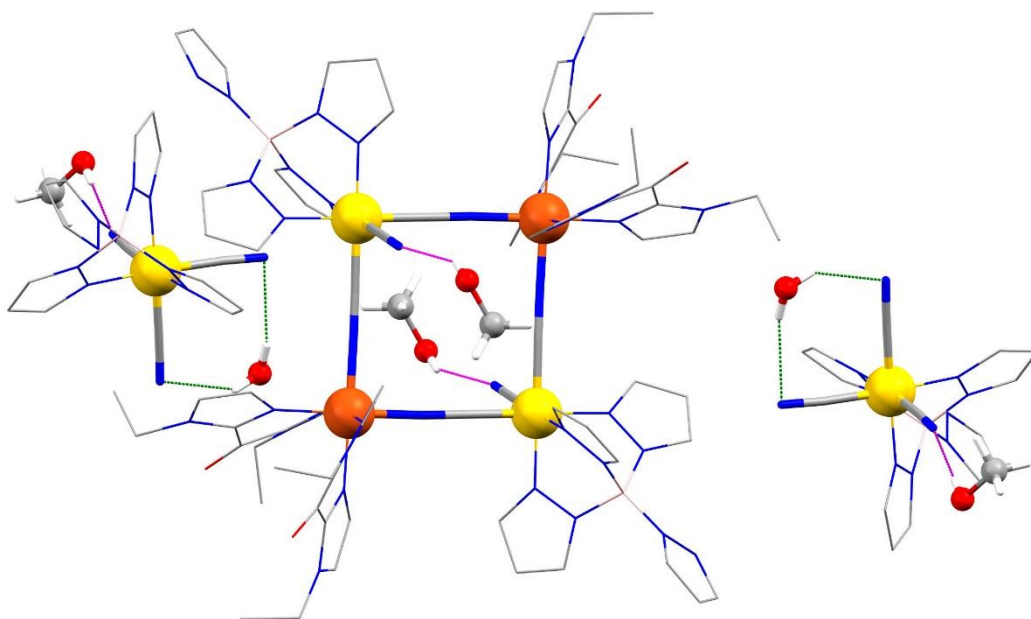


Fig. S6 Perspective view of H-bonding $\text{OH} \cdots \text{N}$ interaction in $1 \cdot 4\text{MeOH} \cdot 2\text{H}_2\text{O}$. The green and magenta dotted line represent H-bonding interactions involved with H_2O and MeOH respectively. (Fe(II), orange; Fe(III), yellow; C, gray; N, blue; O, red and B, light pink). Atoms shown in wireframe style are for clarity. H-atoms other than H-bonding interactions are omitted for clarity.

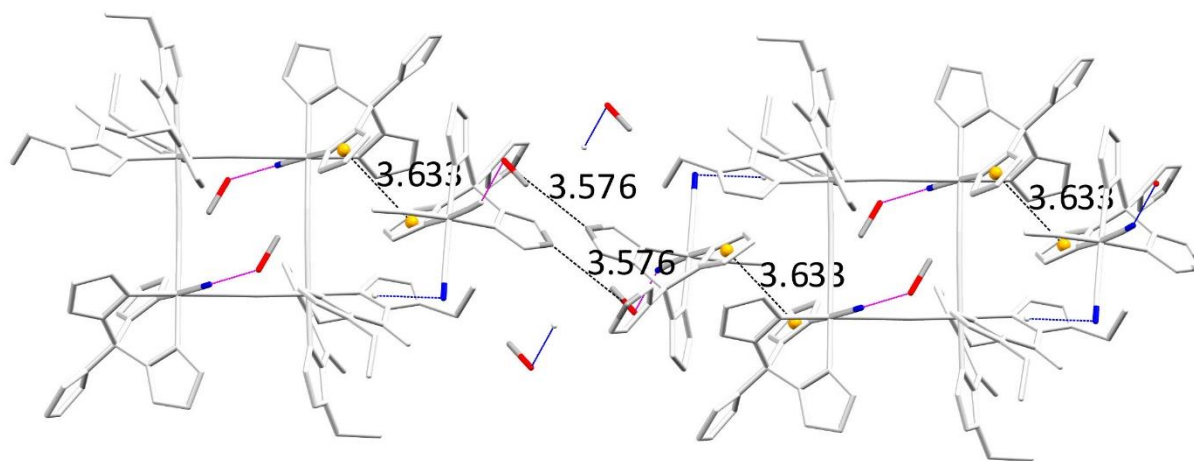


Fig. S7 Perspective view of crystal packing in $1 \cdot 4\text{MeOH} \cdot 2\text{H}_2\text{O}$ showing supramolecular interactions (C-H...C, C-H...N, C-H...O, π - π stacking) between square motifs. π - π stacking between pyrazole rings of pzTp ligands showed in black dotted line (3.633 Å) through yellow colored centroid. CH... π interactions among counter anions are presented in black dotted line with 3.576 Å distance. Magenta and blue dotted line are the H-bonding interactions involving MeOH and H₂O respectively. H-atoms are omitted for clarity.

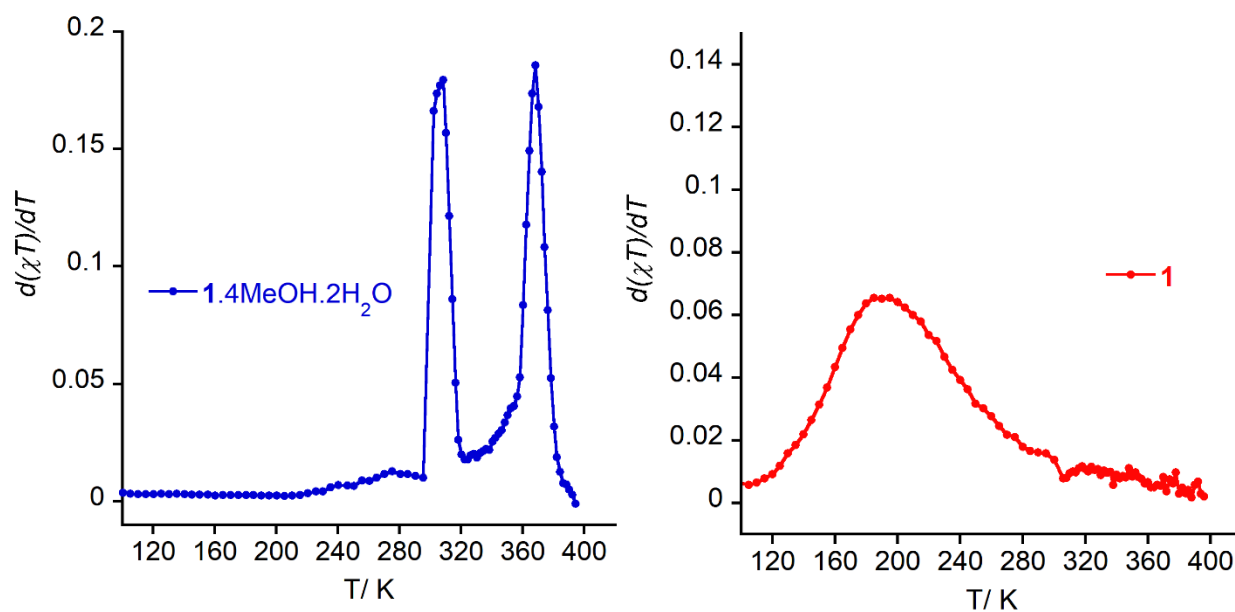


Fig. S8 The first derivative of χT against the temperature, $d(\chi T) / dT$ vs. T in the temperature range of 100 K to 400 K for $1 \cdot 4\text{MeOH} \cdot 2\text{H}_2\text{O}$ and **1** (from left to right).

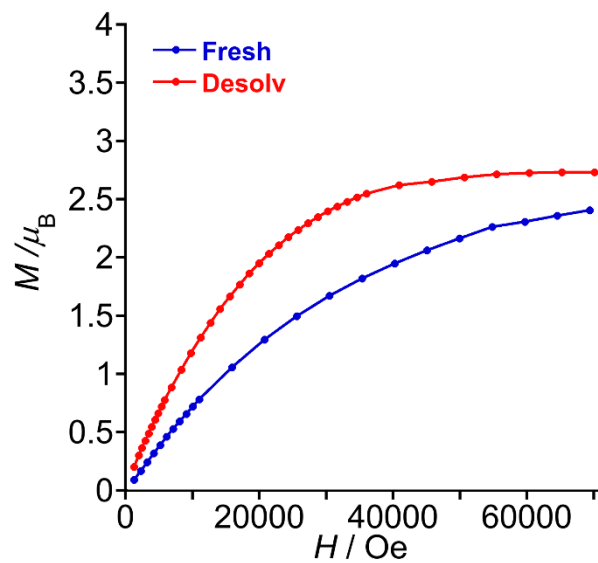


Fig. S9 M vs. H plot for $1 \cdot 4MeOH \cdot 2H_2O$ (red curve) and 1 (blue curve) measured at 2 K. The solid lines are guide for the eyes.

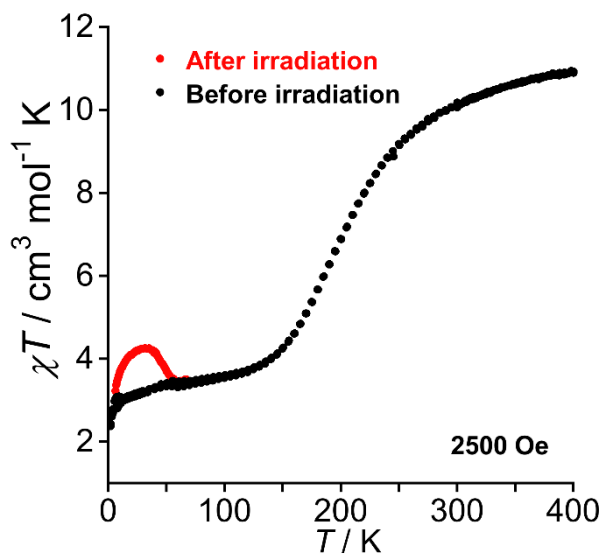


Fig. S10 χT vs. T plots of 1 before and after the 808 nm light irradiation for 230 min at 20 K, 2500 Oe dc field while heating the sample with 0.5 K/min sweep rate.

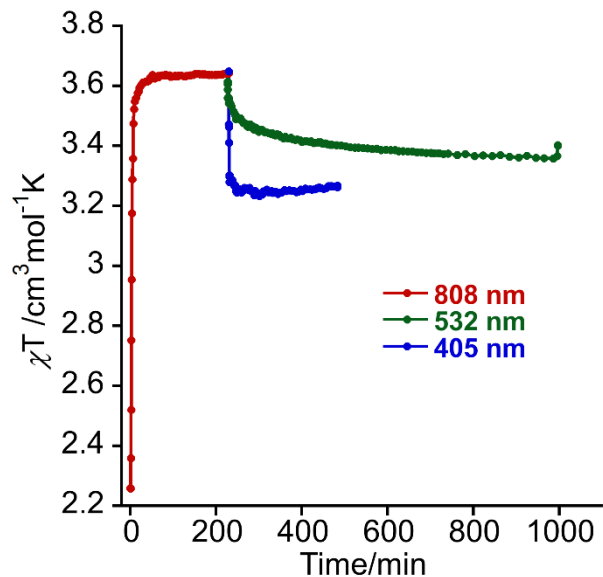


Fig. S11 χT vs. time plots of the photo-induced metastable state of **1** under the 532 nm (green) and 405 nm (blue) laser light irradiation.

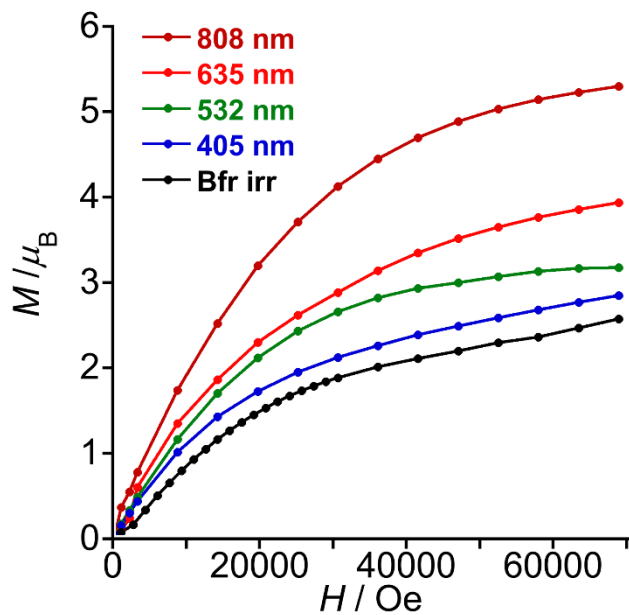


Fig. S12 M vs. H curves of **1** at 2 K before irradiation (black) and after irradiation with 405 nm (blue), 532 nm (green), 635 nm (red), 808 nm (dark red) laser light irradiation at 20 K. The solid lines are guide for the eyes.

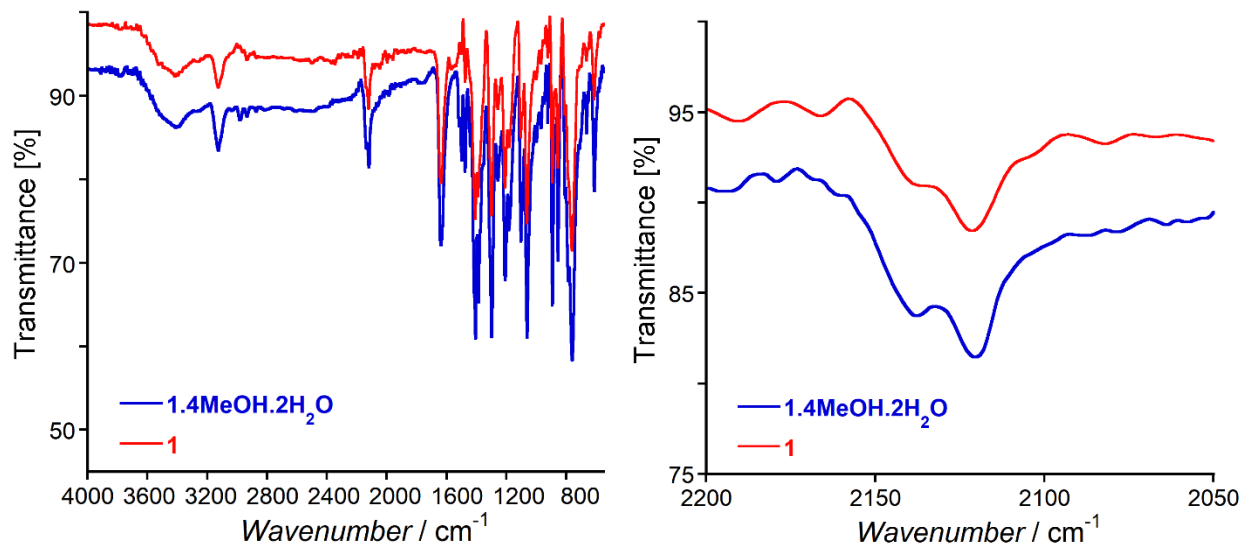


Fig. S13 Solid state FT-IR spectra of 1.4MeOH.2H₂O and 1 in ATR mode in the region of 4000 to 550 cm⁻¹ at room temperature (300 K).

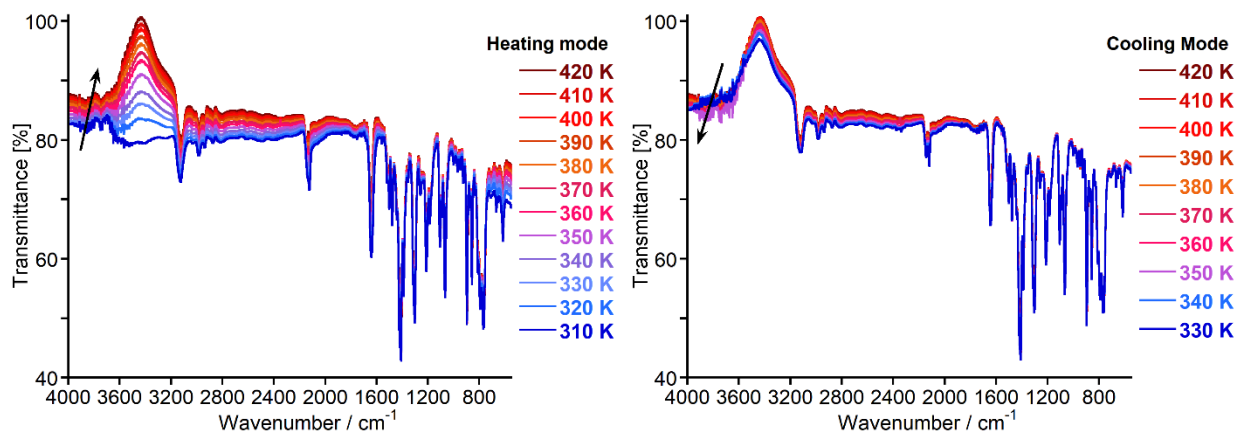


Fig. S14 Variable temperature solid state FT-IR spectra of 1.4MeOH.2H₂O in the temperature range of 310 K – 420 K from 4000 to 550 cm⁻¹ in KBr pellet. Left: Heating mode, and right: cooling mode. Upward and downward arrows signify the heating and cooling mode respectively.

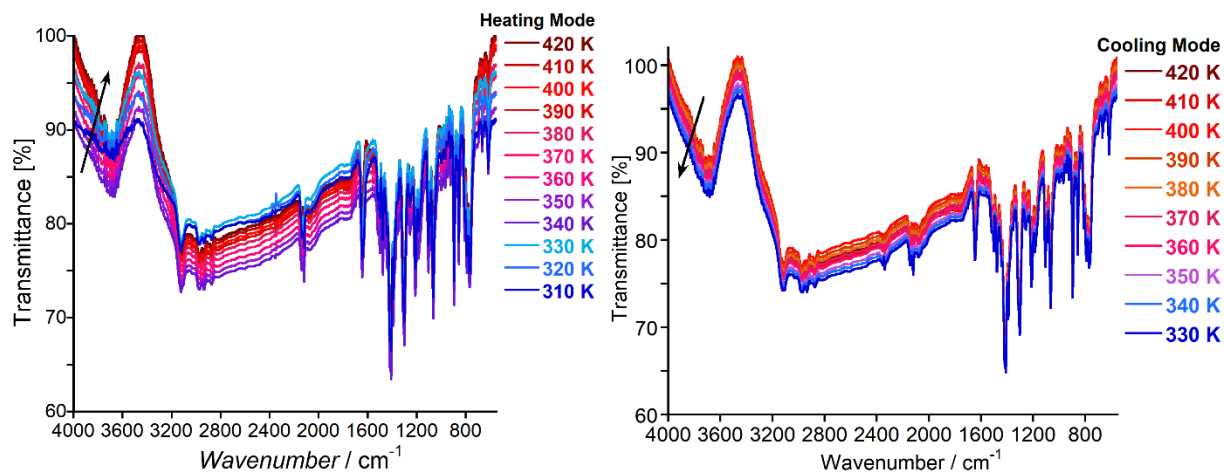


Fig. S15 Variable temperature solid state FT-IR spectra of **1** in the temperature range of 310 K – 420 K from 4000 to 550 cm^{-1} in KBr pellet. Left: Heating mode, and right: cooling mode. Upward and downward arrows signify the heating and cooling mode respectively.

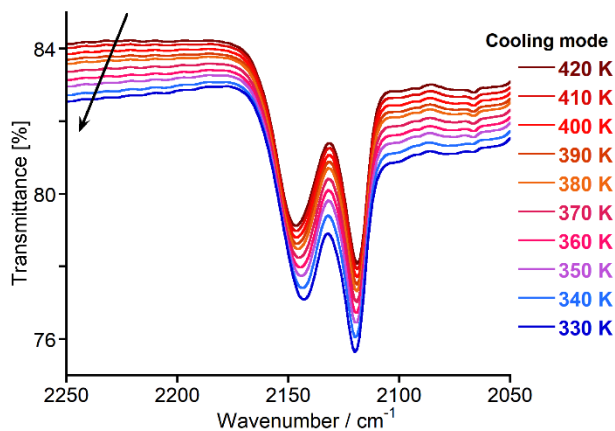


Fig. S16 Variable temperature solid state FT-IR spectra of **1·4MeOH·2H₂O** in the temperature range of 310 K – 420 K from 2250 to 2050 cm^{-1} in KBr pellet in cooling mode. Upward and downward arrows signify the heating and cooling mode, respectively.

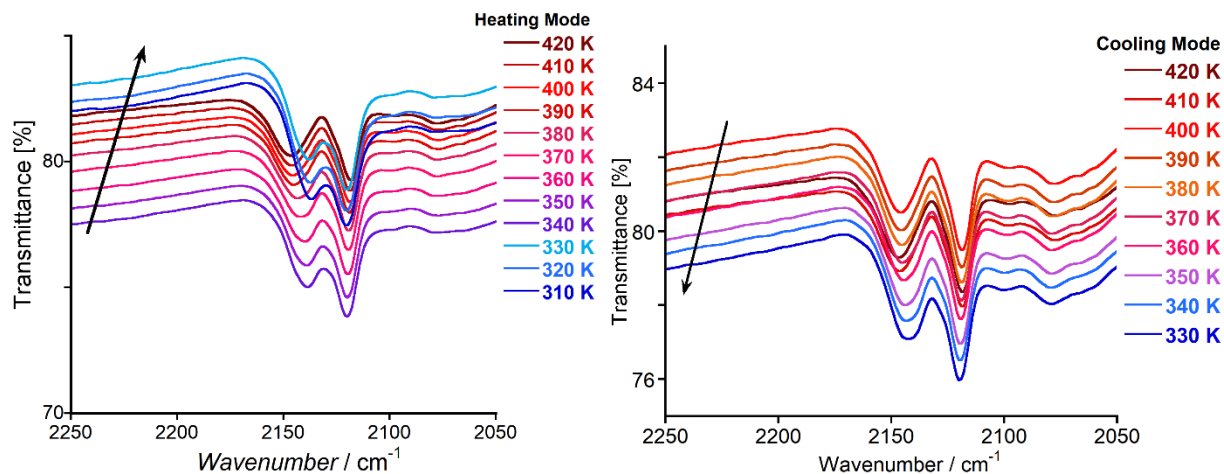


Fig. S17 Variable temperature solid state FT-IR spectra of **1** in the temperature range of 310 K – 420 K from 2250 to 2050 cm^{-1} in KBr pellet method. Left: Heating mode, and right: cooling mode. Upward and downward arrows signify the heating and cooling mode, respectively.

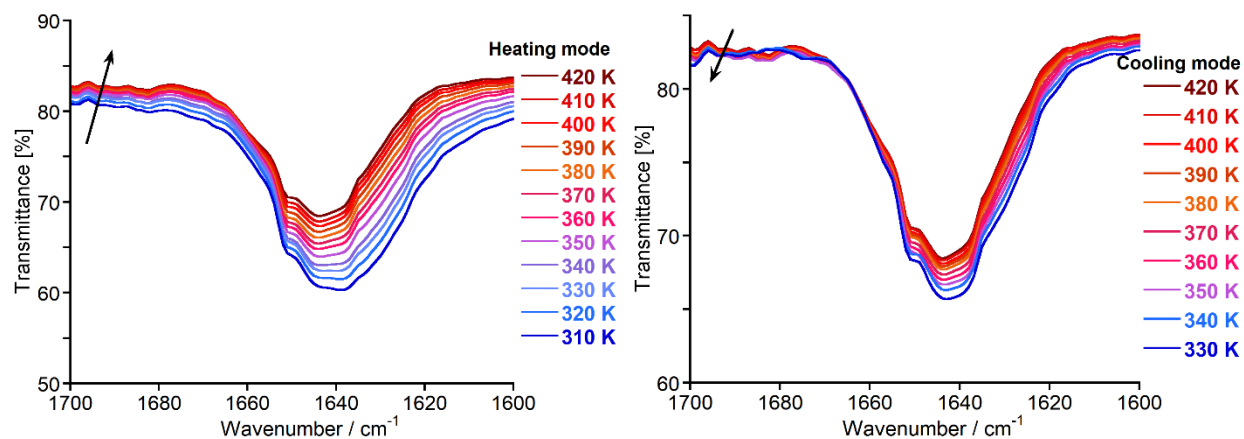


Fig. S18 Variable temperature solid state FT-IR spectra of **1·4MeOH·2H₂O** in the temperature range of 310 K – 420 K from 1700 to 1600 cm^{-1} in KBr pellet. Left: Heating mode, and right: cooling mode. Upward and downward arrows signify the heating and cooling mode, respectively.

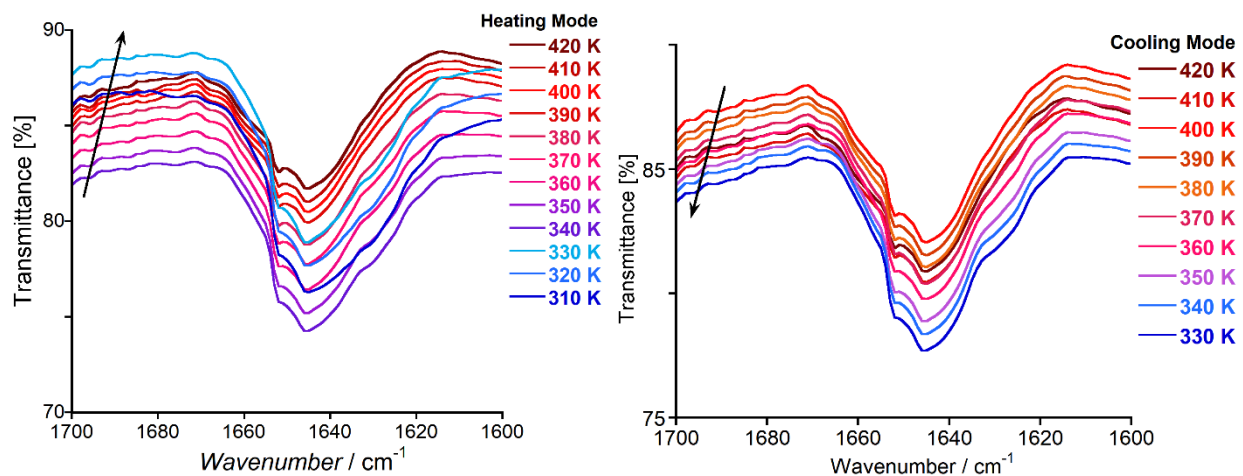


Fig. S19 Variable temperature solid state FT-IR spectra of **1** in the temperature range of 310 K – 420 K from 1700 to 1600 cm^{-1} in KBr pellet. Left: Heating mode, and right: cooling mode. Upward and downward arrows signify the heating and cooling mode, respectively.

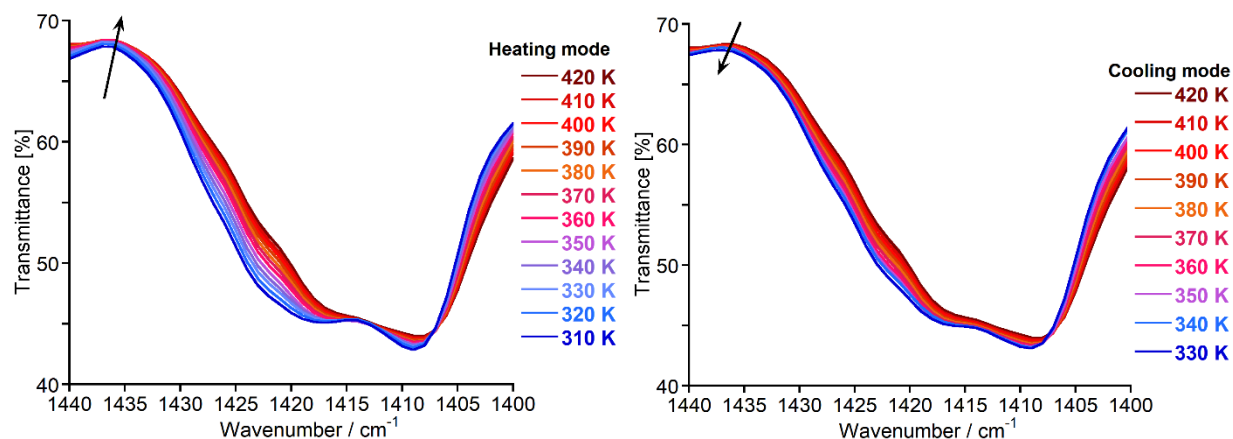


Fig. S20 Variable temperature solid state FT-IR spectra of **1·4MeOH·2H₂O** in the temperature range of 310 K – 420 K from 1440 to 1400 cm^{-1} in KBr pellet. Left: Heating mode, and right: cooling mode. Upward and downward arrows signify the heating and cooling mode, respectively.

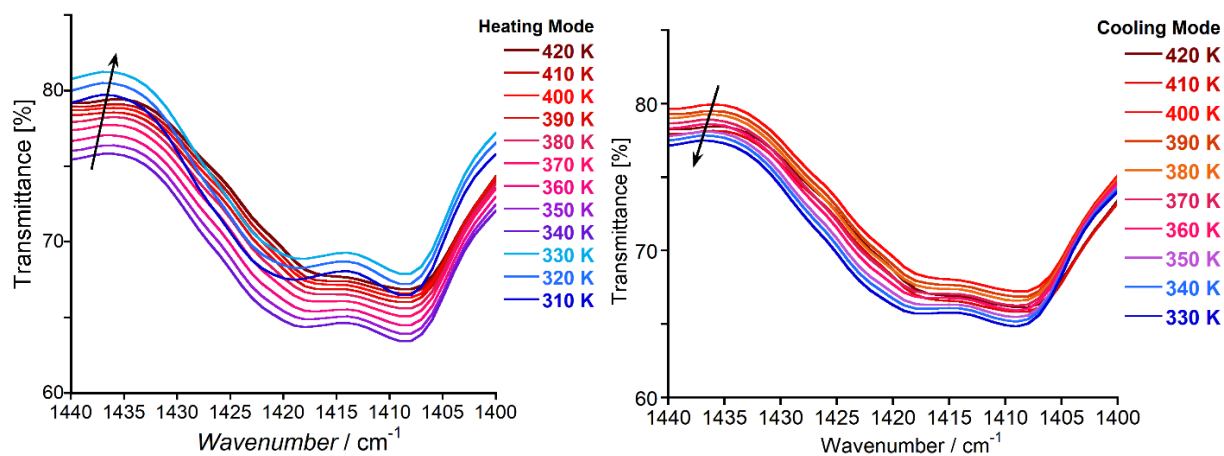


Fig. S21 Variable temperature solid state FT-IR spectra of **1** in the temperature range of 310 K – 420 K from 1440 to 1400 cm^{-1} in KBr pellet method. Left: Heating mode, and right: cooling mode. Upward and downward arrows signify the heating and cooling mode, respectively.

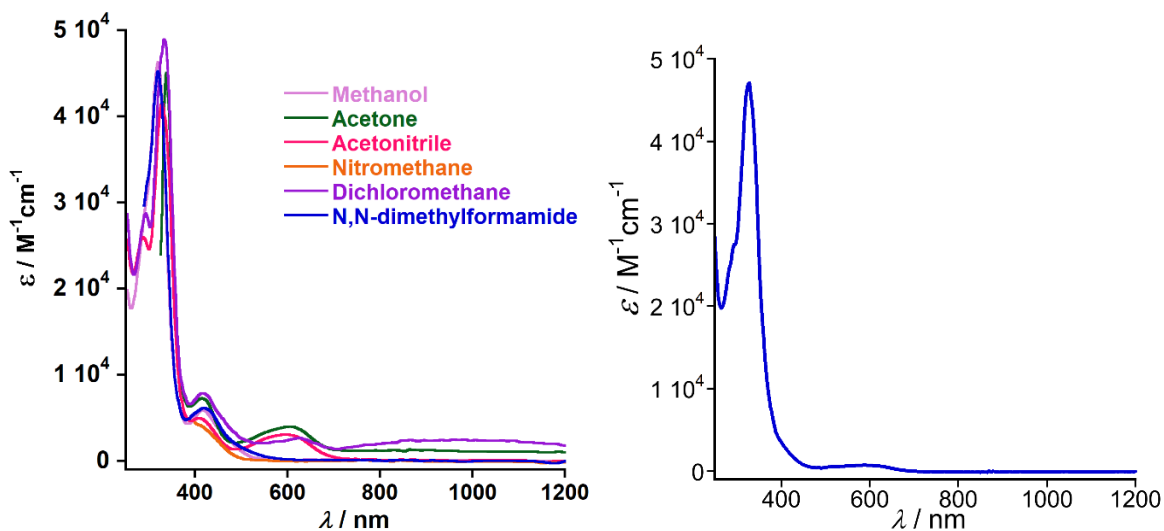


Fig. S22 Compared solution state UV/vis/NIR spectra of $1 \cdot 4\text{MeOH} \cdot 2\text{H}_2\text{O}$ in different solvents with concentration of $\approx 10^{-4}$ (M) at RT (300 K) (left) and solution state UV/vis/NIR spectrum of $[\text{Fe}^{\text{II}}(\text{bik}^*)_3](\text{BF}_4)_2$ (right).

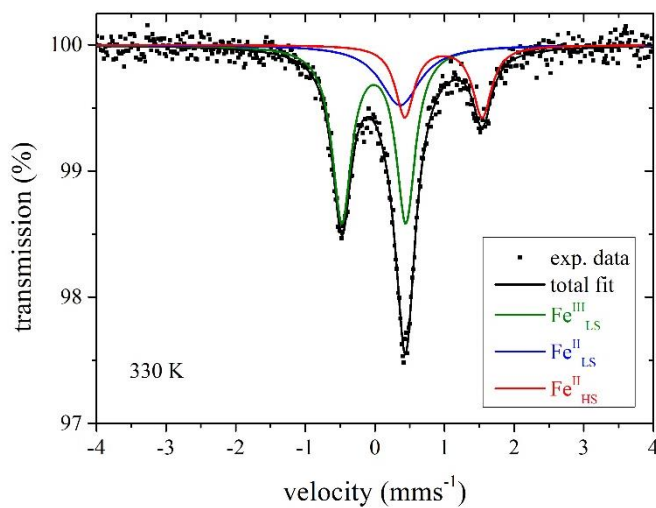


Fig. S23 Mössbauer spectrum of $1 \cdot 4\text{MeOH} \cdot 2\text{H}_2\text{O}$ at 330 K. The green, blue and red curves represent the quadrupole doublets of the LS-Fe(III), LS-Fe(II) and HS-Fe(II) ions, respectively.

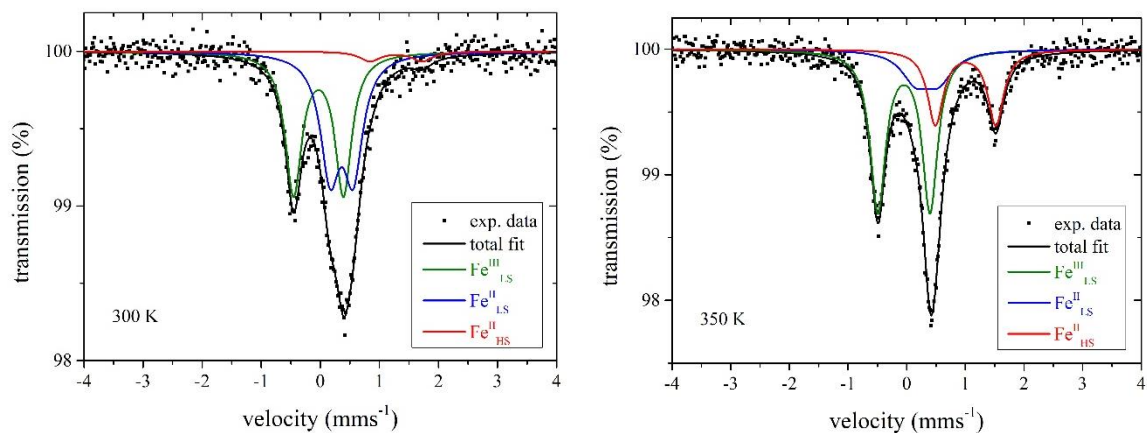


Fig. S24 Mössbauer spectrum of **1** at 300 K (left) and 350 K (right). The green, blue and red curves represent the quadrupole doublets of the LS-Fe(III), LS-Fe(II) and HS-Fe(II) ions, respectively

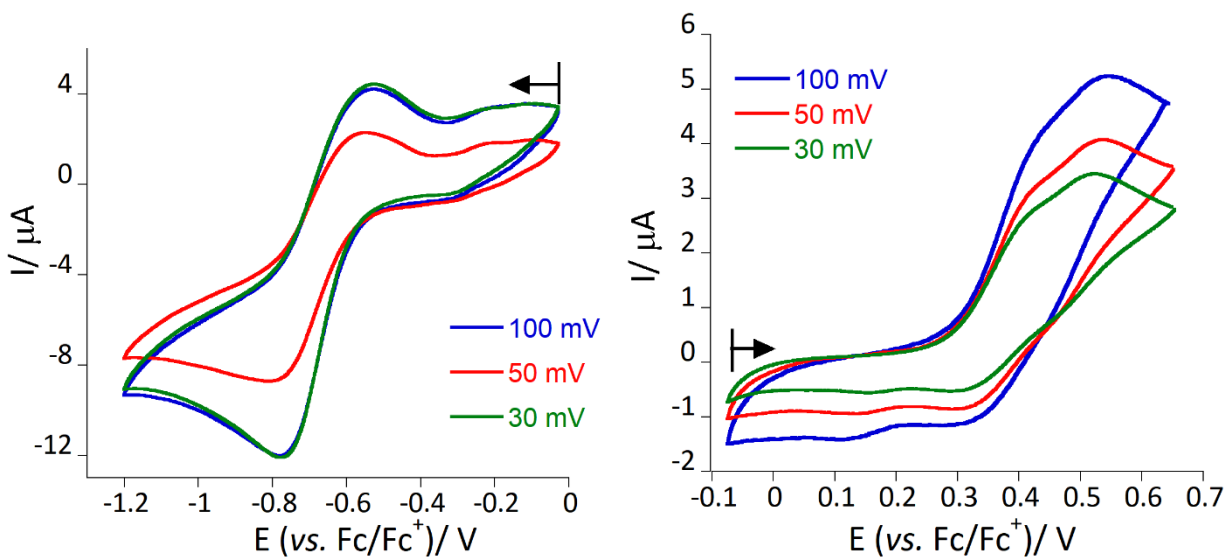


Fig. S25 Cyclic voltammograms of **1**·4MeOH·2H₂O for reduction cycle (left) and oxidation cycle (right) in 0.1 M TBAPF₆/acetonitrile with different scan rate. Arrows indicate the direction of the potential sweep.

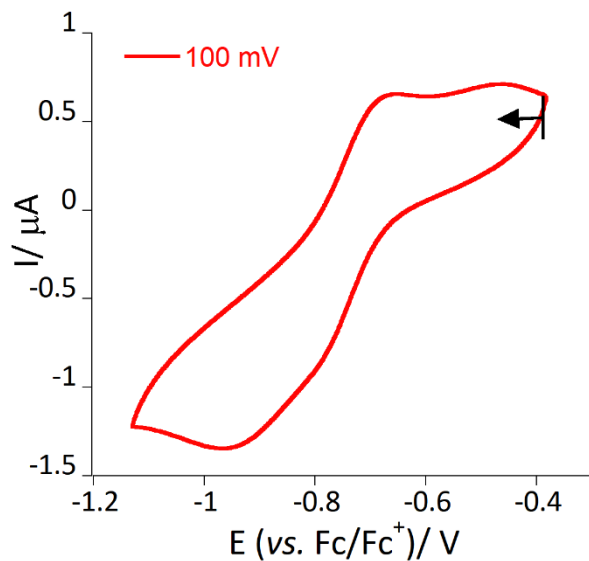


Fig. S26 Cyclic voltammogram of $(\text{PPh}_4)[\text{Fe}^{\text{III}}(\text{pzTp})(\text{CN})_3]$ in 0.1 M $\text{TBAPF}_6/\text{acetonitrile}$ with a scan rate of 0.1 V s^{-1}

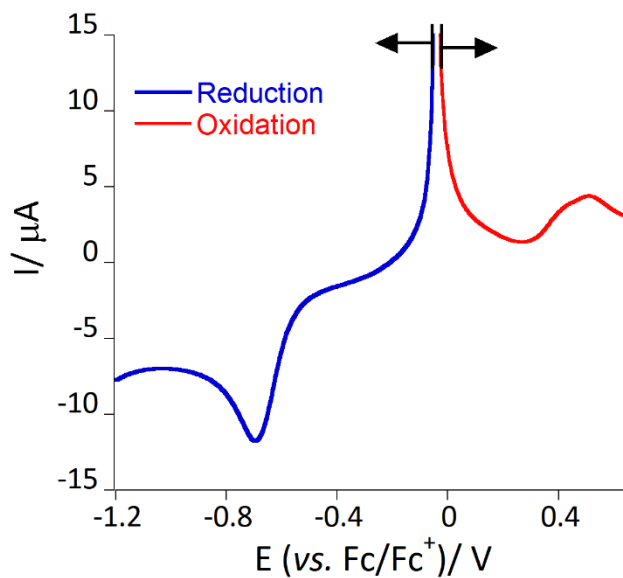


Fig. S27 Square wave voltammograms for $1 \cdot 4\text{MeOH} \cdot 2\text{H}_2\text{O}$ in 0.1 M $(\text{TBA})\text{PF}_6/\text{acetonitrile}$. Arrows indicate the direction of potential sweep.

Table S1 X-ray Crystallography data of 1·4MeOH·2H₂O.

Empirical formula	C ₇₄ H ₈₂ B ₂ Fe ₄ N ₃₈ O ₄ , 2(C ₁₅ H ₁₂ BFeN ₁₁), 4(CH ₄ O), 2(H ₂ O)
Formula weight /g mol ⁻¹	2801
Temperature / K	120
Crystal system	Triclinic
Space group	P-1
<i>a</i> , Å	11.9811(5)
<i>b</i> , Å	14.8759(6)
<i>c</i> , Å	18.5704(8)
α , °	87.675(4)
β , °	78.345(3)
γ , °	79.489(3)
<i>V</i> , Å ³	3187.1(2)
<i>Z</i>	1
<i>d</i> _{cal} , g cm ⁻³	1.462
μ , mm ⁻¹	0.746
<i>F</i> (000)	1452
θ _{max} , °	30.594
Completeness	0.91
Reflections collected	17770 / 19606
Independent reflections	7812
Goodness-of-fit on <i>F</i> ²	0.997
Final R1 indices [<i>I</i> > 2 σ (<i>I</i>)]	0.0859
Final wR2 indices [all data]	0.2638
CCDC	2252523

Continuous Shape Measures (CShM) Analysis

Continuous Shape Measures (CShM) analysis⁸ was carried out to determine the geometry around different iron centers. Based on the values obtained, the idealized polyhedron was matched with the actual coordination spheres. The smallest value is symbolic of proximity of actual coordination sphere and idealized polyhedron.

Table S2 CShM analyses data for 1·4MeOH·2H₂O.

	120 K				
	HP - 6	PPY - 6	OC - 6	TPR - 6	JPPY - 6
Fe1	32.172	29.186	0.093	15.953	32.857
Fe2	33.054	29.218	0.044	15.676	32.724
Fe3	31.873	28.062	0.201	14.284	31.831

HP – 6: Hexagon (D_{6h}), PPY – 6 = Pentagonal pyramid, OC – 6: Octahedron (O_h), TPR – 6: Trigonal prism (D_{3h}), JPPY – 6 = Johnson pentagonal pyramid J₂ (C_{5v})

Table S3 Octahedral distortion parameter calculation for 1·4MeOH·2H₂O.

120 K	<D>	ζ	Δ	Σ	Θ
Fe1	1.9407	0.136569	0.000151	24.9622	65.4529
Fe 2	1.9591	0.082486	0.000062	15.9983	41.4116
Fe 3	1.9459	0.141494	0.000192	33.3887	100.4130

Mean distance (<D>)= d_{mean} , Distance distortion (ζ) = $\sum_{i=1}^6 |d_i - d_{\text{mean}}|$, Tilting distortion parameter (Δ) = $\frac{1}{6} \sum_{i=1}^6 \left(\frac{d_i - d_{\text{mean}}}{d_{\text{mean}}}\right)^2$, Angle distortion (Σ) = $\sum_{i=1}^{12} |90 - \phi_i|$, Torsional distortion (Θ) = $\sum_{i=1}^{24} |60 - \theta_i|$

Table S4 Selected bond lengths (Å) in 1·4MeOH·2H₂O.

1·4MeOH·2H₂O	
	120 K
Fe1-C1	1.917(6)
Fe1-C2	1.923(6)
Fe1-C3	1.915(6)
Fe1-N4	1.952(4)
Fe1-N6	1.964(5)
Fe1-N8	1.974(4)
Fe2-N1	1.947(5)
Fe2-N3	1.930(5)
Fe2-N12	1.970(5)
Fe2-N14	1.969(5)
Fe2-N16	1.966(5)
Fe2-N18	1.971(5)
Fe3-C38	1.926(6)
Fe3-C39	1.929(7)
Fe3-C40	1.914(7)
Fe3-N23	1.990(5)
Fe3-N25	1.945(5)
Fe3-N27	1.974(5)

Table S5 Selected bond angles (°) in 1·4MeOH·2H₂O at 120 K.

	120 K
C1-Fe1-C2	85.9(2)
C1-Fe1-C3	89.0(2)
C1-Fe1-N4	179.1(2)
C1-Fe1-N6	91.9(2)
C1-Fe1-N8	92.8(2)
C2-Fe1-C3	88.4(2)
C2-Fe1-N4	93.2(2)
C2-Fe1-N6	91.8(2)
C2-Fe1-N8	178.7(2)
C3-Fe1-N4	91.2(2)
C3-Fe1-N6	179.1(2)
C3-Fe1-N8	91.5(2)
N4-Fe1-N6	87.90(19)
N4-Fe1-N8	88.06(19)
N6-Fe1-N8	88.34(19)
N1-Fe2-N3	89.42(18)
N1- Fe2-N12	91.75(19)
N1- Fe2-N14	179.2(2)
N1- Fe2-N16	89.73(18)
N1- Fe2-N18	91.57(19)
N3-Fe2-N12	92.63(19)
N3-Fe2-N14	91.40(19)
N3- Fe2-N16	178.5(2)
N3- Fe2-N18	90.68(19)
N14-Fe2-N12	88.12(19)
N16-Fe2-N12	88.6(2)
N12-Fe2-N18	175.33(19)
N16-Fe2-N14	89.45(19)
N16-Fe2-N18	88.1(2)
N14-Fe2-N18	88.51(19)
N27-Fe3-N23	87.88(19)
N25-Fe3-N23	88.2(2)

N25-Fe3-N27	87.9(2)
C38-Fe3-N23	89.7(2)
C38-Fe3-N27	176.3(2)
C38-Fe3-N25	94.8(2)
C38-Fe3-C39	88.1(2)
C39-Fe3-N23	177.6(2)
C39-Fe3-N27	94.4(2)
C39-Fe3-N25	91.1(2)
C40-Fe3-N23	94.6(2)
C40-Fe3-N27	91.7(2)
C40-Fe3-N25	177.1(2)
C40-Fe3-C38	85.7(3)
C40-Fe3-C39	86.0(3)
Fe1-C1-N1	176.3(5)
Fe1-C2-N2	179.3(6)
Fe1-C3-N3	176.9(5)
Fe2-N1-C1	178.4(5)
Fe2-N3-C3	176.2(4)
Fe3-C38-N20	177.1(6)
Fe3-C39-N21	177.6(6)
Fe3-C40-N22	176.2(6)
Fe1-Fe2-Fe1	89.74(2)
Fe2-Fe1-Fe2	90.25(3)

Table S6 Mössbauer spectroscopy data for 1·4MeOH·2H₂O and **1** at different temperatures.

Complex	Temperature	δ (mms ⁻¹) ± 0.02	ΔE_Q (mms ⁻¹) ± 0.02	Area (%) ± 1	Remarks
1·4MeOH·2H ₂ O	100 K	0.44	0.35	46.3	Fe ^{II} _{LS}
		0.06	1.03	53.7	Fe ^{III} _{LS}
	300 K	1.13	1.16	7.4	Fe ^{II} _{HS}
		0.36	0.36	37.8	Fe ^{II} _{LS}
	330 K	-0.04	0.86	54.7	Fe ^{III} _{LS}
		0.99	1.11	22.9	Fe ^{II} _{HS}
1	300 K	0.36	0.39	46.7	Fe ^{II} _{LS}
		-0.03	0.84	49	Fe ^{III} _{LS}
		1.00	1.03	26.7	Fe ^{II} _{HS}
	350 K	0.35	0.39	18.2	Fe ^{II} _{LS}
		-0.05	0.89	55.1	Fe ^{III} _{LS}

The uncertainty of hyperfine parameters determination (isomer shift δ and quadrupole splitting ΔE_Q) is ± 0.02 mms⁻¹ (unless otherwise specified, as a result of fitting process in MossWinn).

2. References

1. Y.-Z. Zhang, P. Ferko, D. Siretanu, R. Ababei, N. P. Rath, M. J. Shaw, R. Clérac, C. Mathonière and S. M. Holmes, *J. Am. Chem. Soc.*, 2014, **136**, 16854-16864.
2. S. De, S. Tewary, D. Garnier, Y. Li, G. Gontard, L. Lisnard, A. Flambard, F. Breher, M.-L. Boillot, G. Rajaraman and R. Lescouëzec, *Eur. J. Inorg. Chem.*, 2018, **2018**, 414-428.
3. S. Ghosh, S. Kamilya, M. Das, S. Mehta, M. E. Boulon, I. Nemeč, M. Rouzies, R. Herchel and A. Mondal, *Inorg. Chem.*, 2020, **59**, 7067-7081.
4. G. M. Sheldrick, *Journal*, Madison, WI, 1996.
5. G. Sheldrick, *Acta Crystallogr., Sect. C: Struct. Chem*, 2015, **71**, 3-8.
6. O. V. Dolomanov, L. J. Bourhis, R. J. Gildea, J. A. K. Howard and H. Puschmann, *J. Appl. Crystallogr.*, 2009, **42**, 339-341.
7. T. Degen, M. Sadki, E. Bron, U. König and G. Nénert, *Powder Diffr.*, 2014, **29**, S13-S18.
8. M. Pinsky and D. Avnir, *Inorg. Chem.*, 1998, **37**, 5575-5582.